







Article

Development of Thermo- and pH-Sensitive Liposomal Magnetic Carriers for New Potential Antitumor Thienopyridine Derivatives

Beatriz C. Ribeiro ¹, Cristina A. R. Alvarez ¹, Bárbara C. Alves ¹, Juliana M. Rodrigues ² , Maria João R. P. Queiroz ² , Bernardo G. Almeida ¹, Ana Pires ³, André M. Pereira ³, João P. Araújo ³ , Paulo J. G. Coutinho ¹ , Ana Rita O. Rodrigues ^{1,*}  and Elisabete M. S. Castanheira ^{1,*} 

¹ Centre of Physics of Minho and Porto Universities (CF-UM-UP), Campus de Gualtar, University of Minho, 4710-057 Braga, Portugal; pg37976@alunos.uminho.pt (B.C.R.); pg46653@alunos.uminho.pt (C.A.R.A.); pg46652@alunos.uminho.pt (B.C.A.); bernardo@fisica.uminho.pt (B.G.A.); pcoutinho@fisica.uminho.pt (P.J.G.C.)

² Centre of Chemistry (CQUM), University of Minho, Campus de Gualtar, 4710-057 Braga, Portugal; juliana.mourarodrigues@gmail.com (J.M.R.); mjrpq@quimica.uminho.pt (M.J.R.P.Q.)

³ IFIMUP-Instituto de Física dos Materiais, Universidade do Porto, Rua do Campo Alegre, 4169-007 Porto, Portugal; ana.pires@fc.up.pt (A.P.); amperreira@fc.up.pt (A.M.P.); jearaujo@fc.up.pt (J.P.A.)

* Correspondence: ritarodrigues@fisica.uminho.pt (A.R.O.R.); ecoutinho@fisica.uminho.pt (E.M.S.C.)



Citation: Ribeiro, B.C.; Alvarez, C.A.R.; Alves, B.C.; Rodrigues, J.M.; Queiroz, M.J.R.P.; Almeida, B.G.; Pires, A.; Pereira, A.M.; Araújo, J.P.; Coutinho, P.J.G.; et al. Development of Thermo- and pH-Sensitive Liposomal Magnetic Carriers for New Potential Antitumor Thienopyridine Derivatives. *Materials* **2022**, *15*, 1737. <https://doi.org/10.3390/ma15051737>

Academic Editor: Ovidiu Oprea

Received: 30 January 2022

Accepted: 23 February 2022

Published: 25 February 2022

Publisher's Note: MDPI stays neutral with regard to jurisdictional claims in published maps and institutional affiliations.



Copyright: © 2022 by the authors. Licensee MDPI, Basel, Switzerland. This article is an open access article distributed under the terms and conditions of the Creative Commons Attribution (CC BY) license (<https://creativecommons.org/licenses/by/4.0/>).

Abstract: The development of stimuli-sensitive drug delivery systems is a very attractive area of current research in cancer therapy. The deep knowledge on the microenvironment of tumors has supported the progress of nanosystems' ability for controlled and local fusion as well as drug release. Temperature and pH are two of the most promising triggers in the development of sensitive formulations to improve the efficacy of anticancer agents. Herein, magnetic liposomes with fusogenic sensitivity to pH and temperature were developed aiming at dual cancer therapy (by chemotherapy and magnetic hyperthermia). Magnetic nanoparticles of mixed calcium/manganese ferrite were synthesized by co-precipitation with citrate and by sol-gel method, and characterized by X-ray diffraction (XRD), scanning electron microscopy in transmission mode (STEM), and superconducting quantum interference device (SQUID). The citrate-stabilized nanoparticles showed a small-sized population (around 8 nm, determined by XRD) and suitable magnetic properties, with a low coercivity and high saturation magnetization (~54 emu/g). The nanoparticles were incorporated into liposomes of dipalmitoylphosphatidylcholine/cholesterol hemisuccinate (DPPC:CHEMS) and of the same components with a PEGylated lipid (DPPC:CHEMS:DSPE-PEG), resulting in magnetoliposomes with sizes around 100 nm. Dynamic light scattering (DLS) and electrophoretic light scattering (ELS) measurements were performed to investigate the pH-sensitivity of the magnetoliposomes' fusogenic ability. Two new antitumor thienopyridine derivatives were efficiently encapsulated in the magnetic liposomes and the drug delivery capability of the loaded nanosystems was evaluated, under different pH and temperature conditions.

Keywords: magnetic nanoparticles; mixed ferrite; magnetoliposomes; pH sensitive; thienopyridine derivatives; antitumor compounds; cancer therapy

1. Introduction

Tumors are characterized by a specific microenvironment due to the uncontrolled cell proliferation, acidic pH, overexpression of proteins and enzymes and high levels of oxidation/deoxidation, as a result of the peculiar nutritional environment and of the metabolic pattern change of tissues. Based on these characteristics, endogenous and exogenous stimuli have been strategically studied as triggers in the development of controlled drug-delivery nanosystems [1,2]. Endogenous triggers are regulated by the diseased tissue

microenvironment, while exogenous ones can be modulated by external factors, and thus precisely controlled. Nanosystems with responsive profiles to the pH, redox, enzyme and ionic microenvironment have been the most reported endogenous triggers. On the other hand, the most used exogenous triggers are temperature, magnetic field, light, electric field and ultrasound [3]. Magnetic fields can precisely control heat generation to induce drug release from thermo-responsive nanosystems, while overheating cancer cells [4,5]. Under AC magnetic field, superparamagnetic nanoparticles are able to produce heat, and nanosystems based on magnetic nanoparticles are ideal for temperature-controlled drug delivery and simultaneous hyperthermia. Metal ferrite nanoparticles are promising for their high saturation magnetization, low hysteresis and chemical stability. Among all ferrites, manganese ferrite nanoparticles have been reported as novel agents for magnetic hyperthermia for their tunable magnetic properties [6]. The magnetic properties of metal ferrites with spinel structure strongly depend on the nature of the ions and their distribution among tetrahedral and octahedral sites. Hence, doping spinel ferrites with non-toxic and non-magnetic elements, such as calcium, alters the distribution of ions in both sites, leading to variation in magnetic properties that can boost magnetization, while promoting a higher biocompatibility [7,8].

The integration of two or more stimuli (endogenous and/or exogenous) into a single nanosystem is very attractive and has been explored to enhance therapeutic efficacy. Multi-responsive drug-delivery nanosystems with different stimuli combinations have been reported [9–11]. Considering the acidic pH of tumors, with the extracellular environment reaching pH values down to 5.7 [12], and the fact that high temperatures can trigger drug release in thermo-sensitive nanosystems, while selectively damaging cancer cells (in the range of 39 °C to 42 °C) [13], the combination of pH and temperature stimuli is a promising approach in cancer treatment. The potential of cholesteryl hemisuccinate (CHEMS) to achieve nanosystems with pH-dependent drug delivery has been investigated. CHEMS is a protonable lipid that is negatively charged at neutral pH and becomes neutral at acidic environment. This weakly acidic amphiphilic molecule possesses polymorphic phase behavior as a function of its protonation state around its pK_a , owning a lamellar stable phase at pH = 7 and an inverted hexagonal phase (H_{II}) at pH = 5 [14]. Hence, in an acidic environment, formulations containing CHEMS become fusogenic. In fact, lipids that undergo the lamellar-to-inverted hexagonal phase support membrane fusion, while phospholipids that undergo the gel-to-liquid crystalline phase promote drug release due to the increased bilayer fluidity and permeability above melting temperature. For thermosensitive formulations, DPPC is one of the most suitable lipids because it has a transition temperature around 41 °C, that is, a few degrees above physiological temperature and in the range of mild hyperthermia temperatures [4]. The effect of CHEMS as a stabilizer of DPPC vesicles shows that the inclusion of a low amount of CHEMS has no significant influence on the transition temperature of the formulation [15].

Hence, multi-stimuli magnetoliposomes of DPPC and CHEMS can be very attractive, due to their ability to be stable in blood circulation and release cargo at target sites by internal (pH) and external (magnetic field) stimuli while performing hyperthermia, which is promising for cancer treatment.

In this work, magnetoliposomes based on the thermosensitive lipid DPPC and the pH-sensitive agent CHEMS were prepared. Magnetic nanoparticles of manganese/calcium ferrite were chosen as the magnetic component. To assess the potential of the developed magnetic liposomes as drug nanocarriers, two novel antitumor thienopyridine derivatives, recently synthesized [16] (Figure 1), were loaded into the nanosystems. The thienopyridine derivatives have been described as antitumor and antiangiogenic agents, as well as inhibitors for tyrosine kinase receptors [17–19].



Figure 1. Structures of the new antitumor compounds (Me: methyl group). Compound A: methyl 3-(pyridin-2-ylethynyl)thieno[3,2-*b*]pyridine-2-carboxylate; Compound B: methyl 3-(*p*-tolylethynyl)thieno[3,2-*b*]pyridine-2-carboxylate.

The two novel compounds were previously assayed in human tumor cell lines [16] (Table 1), namely in colon cancer (HCT-15 cell line) and non-small cell lung cancer (NCI-H460). The results were compared with those for doxorubicin (DOX), a widely-used therapeutic anticancer agent, and revealed much lower growth inhibitory concentrations (GI_{50}) for the new compounds in both tumor cell lines (except for Compound A in NCI-H460 cells). These GI_{50} values, in the nanomolar concentration range, stand out when compared to other thienopyridines [18–22] and to the anticancer DOX, inspiring the assays of encapsulation in magnetoliposomes.

Table 1. Growth inhibitory concentration values ($GI_{50} \pm SD$; SD being the standard deviation) for Compounds A and B and DOX in tumor cells [16].

	HCT-15 (nM)	NCI-H460 (nM)
Compound A	5.6 ± 0.6	>75
Compound B	10.8 ± 1.1	17.0 ± 1.2
Doxorubicin	353.3 ± 24.2	25 ± 0.8

Both compounds were successfully encapsulated in the developed nanosystems, representing promising formulations for application in cancer therapeutics.

2. Materials and Methods

2.1. Preparation of Mixed Calcium/Manganese Ferrite Nanoparticles

Spectroscopic-grade solvents and ultrapure water of Milli-Q grade (MilliporeSigma, St. Louis, MO, USA) were used in all preparations. Iron(III) chloride ($FeCl_3 \cdot 6H_2O$), manganese sulfate ($MnSO_4 \cdot H_2O$) and calcium acetate, $Ca(CH_3COO)_2 \cdot H_2O$ (from Sigma-Aldrich, St. Louis, MO, USA) were used in the synthesis of the mixed calcium/manganese ferrite nanoparticles. ACS-grade reagent trisodium citrate dehydrate and sodium hydroxide solution, 50% in water (from Sigma-Aldrich, St. Louis, MO, USA), were employed in the co-precipitation method. Nitric acid and citric acid (from Sigma-Aldrich, St. Louis, MO, USA) were used in the sol-gel synthesis method.

2.1.1. Co-Precipitation Method

Citrate-stabilized calcium/manganese ferrite NPs, $Ca_{0.5}Mn_{0.5}Fe_2O_4$, were prepared by the co-precipitation method in aqueous solution. First, an aqueous solution of NaOH (2.32 M) and trisodium citrate dehydrate (0.75 M) was prepared and heated up to 90 °C, under vortexing. Then, a mixed solution containing iron(III) chloride 1 M, manganese sulfate 0.25 M and calcium acetate 0.25 M was added drop-by-drop. The mixture was kept under vortexing, at 90 °C, for 2 h. The obtained nanoparticles were washed several times by magnetic decantation with water and ethanol.

2.1.2. Sol-Gel Method

The $Ca_{0.5}Mn_{0.5}Fe_2O_4$ nanoparticles were also synthesized via the sol-gel method under acid-catalyzed conditions. Nitric acid 0.05 M and citric acid 0.15 M were used for

the hydrolysis of the metal precursor mixture. A mixed solution of iron(III) chloride 1 M, manganese sulfate 0.25 M and calcium acetate 0.25 M, was added to the acids and slowly heated at 90 °C, under magnetic stirring, to form a xerogel. After formation of the dry gel, the temperature was raised to 250 °C, until a powder was obtained. The purification process was performed by several cycles of centrifugation, washing with water and ethanol. Finally, the obtained nanoparticles were subjected to calcination at 300 °C for 3 h.

2.2. Synthesis of Magnetic Liposomes and Small Unilamellar Vesicles

Magnetic liposomes based on $\text{Ca}_{0.5}\text{Mn}_{0.5}\text{Fe}_2\text{O}_4$ nanoparticles were obtained by the ethanolic injection method, as previously described [23,24]. Briefly, an ethanolic solution of 1×10^{-3} M total lipid concentration was injected, drop by drop, into a nanoparticle aqueous solution (1×10^{-4} M) at 55 °C under vortexing. The non-encapsulated nanoparticles were removed through magnetic decantation. Different formulations containing the thermosensitive lipid DPPC (dipalmitoylphosphatidylcholine), the pH-sensitive agent cholesteryl hemisuccinate (CHEMS) and the PEGylated lipid distearoylphosphatidylethanolamine-*N*-[methoxy(polyethylene glycol)-2000] (ammonium salt) (DSPE-PEG) were prepared, specifically DPPC (100%), DPPC:CHEMS (molar ratio 80:20) and DPPC:CHEMS:DSPE-PEG (molar ratio 80:20:0.4). All components were purchased from Sigma-Aldrich (St. Louis, MO, USA).

The two novel antitumor thienopyridine derivatives were encapsulated into the magnetoliposomes by co-injection of the compound with the lipid solution (final compound concentration: 1×10^{-6} M), an efficient method for encapsulation of hydrophobic compounds [25].

Small unilamellar vesicles (SUVs) were used as models of cell membranes, and their interaction with the developed magnetoliposomes was studied. SUVs of egg-phosphatidylcholine, Egg-PC (from Sigma-Aldrich, St. Louis, MO, USA) were also prepared by ethanolic injection method.

2.3. Structural Characterization

The composition and crystalline phases of the synthesized nanoparticles were evaluated by the XRD (X-Ray Diffraction) technique, using a PAN'alytical X'Pert PRO diffractometer, operating with $\text{CuK}\alpha$ radiation and Bragg–Brentano configuration, at the Electron Microscopy Unit, University of Trás-os-Montes and Alto Douro (UTAD), Vila Real, Portugal.

Scanning electron microscopy images were recorded using a NanoSEM-FEI Nova 200 (FEI Technologies, Inc., Hillsboro, OR, USA), operating in transmission mode (STEM), at SEMAT (Serviços de Caracterização de Materiais, Guimarães, Portugal). The software *ImageJ* (National Institutes of Health (NIH), version 1.53c, Bethesda, MD, USA) was used to process STEM images by increasing contrast and subtracting background. Then, a manual outline of the nanoparticles with the best-defined limit was performed (~150 counts) using the ROI (Region of Interest) manager tool, and the sizes were estimated considering the area of the circle.

The size (hydrodynamic diameter) and zeta potential of magnetic liposomes were measured using a Dynamic Light Scattering NANO ZS Malvern Zetasizer (Malvern Panalytical Ltd., Malvern, UK) equipped with a He-Ne laser ($\lambda = 632.8$ nm). For each sample, five independent measurements were carried out, to determine mean size and size distribution (polydispersity index).

2.4. Magnetic Measurements

The magnetic properties of the $\text{Ca}_{0.5}\text{Mn}_{0.5}\text{Fe}_2\text{O}_4$ nanoparticles were measured in a MPMS3 SQUID magnetometer MPMS5XL (Quantum Design Inc., San Diego, CA, USA), using applied magnetic fields up to 5 T. The magnetization dependence on magnetic field (hysteresis cycles) was performed by measuring the magnetization at a series of different applied magnetic fields, at room temperature.

2.5. Spectroscopic Measurements

2.5.1. General Methods

The UV-Vis-NIR spectrophotometer Shimadzu UV-3600 Plus (Shimadzu Corporation, Kyoto, Japan) was used to measure the absorption spectra and the spectrofluorimeter Fluorolog 3 (HORIBA Jobin Yvon IBH Ltd., Glasgow, UK), possessing double monochromators in excitation and emission, Glan–Thompson polarizers, and a temperature-controlled sample holder, was used to measure the emission spectra.

2.5.2. Fluorescence Anisotropy Measurements

Fluorescence anisotropy studies were performed by measuring the steady-state fluorescence anisotropy (r) [26], calculated by Equation (1)

$$r = \frac{I_{VV} - GI_{VH}}{I_{VV} + 2GI_{VH}}, \quad (1)$$

where I_{VV} and I_{VH} are the intensities of the emission spectra obtained with vertical and horizontal polarization, respectively (using excitation light with vertical polarization). The instrument correction factor (G) is the ratio I_{HV}/I_{HH} , where I_{HV} and I_{HH} are the emission intensities obtained with vertical and horizontal polarization (using excitation light with horizontal polarization).

2.5.3. Compound Encapsulation Efficiency

The encapsulation efficiency, EE(%), of the antitumor compounds in the magnetic nanosystems was determined by using Amicon[®] Ultra centrifugal filter units 100 kDa (Merck Millipore, Darmstadt, Germany) for the separation of encapsulated and non-encapsulated compound. For that, drug-loaded magnetoliposomes were subjected to a 60 min centrifugation at 11,000 rpm and the filtrate (consisting of non-encapsulated drug) fluorescence was measured. Then, the concentration of non-encapsulated compound was determined through a previously obtained calibration curve for each compound (plot of the fluorescence intensity versus compound concentration). For that, the fluorescence intensity was measured and converted to the corresponding compound concentration. For each lipid formulation, three independent measurements were carried out and EE(%) was determined using Equation (2).

$$EE(\%) = \frac{C_{(\text{total compound})} - C_{(\text{non-encapsulated compound})}}{C_{(\text{total compound})}} \times 100 \quad (2)$$

3. Results and Discussion

3.1. Nanoparticle Synthesis and Characterization

3.1.1. X-ray Analysis

$\text{Ca}_{0.5}\text{Mn}_{0.5}\text{Fe}_2\text{O}_4$ NPs were prepared by the co-precipitation method in the presence of citrate (to provide electrostatic stabilization) and by the sol–gel technique. The X-ray diffraction (XRD) pattern of the synthesized nanoparticles was obtained and the data analysis was processed by Rietveld optimization using the Profex/BGMN software [27,28] to identify the sample phases and crystallite sizes. The XRD pattern of the $\text{Ca}_{0.5}\text{Mn}_{0.5}\text{Fe}_2\text{O}_4$ (citrate-stabilized) NPs displayed in Figure 2A shows well-defined peaks, confirming its crystallinity. The needed structure file resulted from the import process of CIF file nr. 2300618 (MnFe_2O_4 , space group Fd-3m) followed by changes in the unit cell composition, so that half the Mn^{2+} positions are occupied by Ca^{2+} while the cation distribution over the tetrahedral and octahedral sites can be varied during the Rietveld optimization. All the identified peaks correspond to the intended phase, confirming its purity, and occurred at 18.2° (1 1 1), 29.9° (2 2 0), 35.3° (3 1 1), 36.9° (2 2 2), 42.9° (4 0 0), 46.9° (3 3 1), 53.2° (4 2 2), 56.7° (5 1 1), 56.7° (3 3 3), 62.3° (4 4 0), 65.5° (5 3 1), 70.6° (6 2 0), 73.7° (5 3 3), 74.7° (6 2 2), 78.6° (4 4 4), 81.5° (7 1 1), 81.5° (5 5 1), 86.3° (6 4 2), 89.2° (7 3 1), 89.2° (5 5 3), 94.0° (8 0 0) and

96.9° (7 3 3). On the other hand, the corresponding XRD of the $\text{Ca}_{0.5}\text{Mn}_{0.5}\text{Fe}_2\text{O}_4$ (sol-gel) NPs (Figure 2B) revealed additional peaks indicating that the sol-gel method results in less pure samples. Almost all of the additional peaks observed match with the hematite phase (Hematite.str included in BGMN structure files), as observed by the identified peaks (filled squares). A percentage of 27.3% of hematite was detected. The success of the sol-gel method relies on the uniform distribution of metal cations within the xerogel, prior to the high-temperature combustion process. The fact that a significant amount of hematite was obtained indicates the presence of iron-enriched regions in the prepared xerogel.

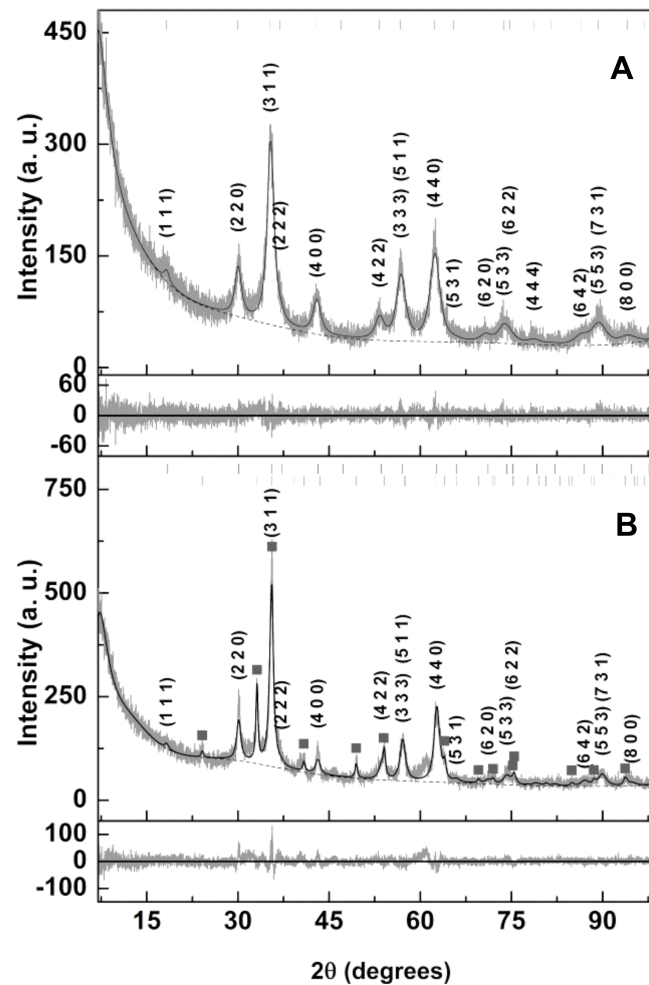


Figure 2. X-Ray diffractogram of (A) citrate-stabilized calcium/manganese ferrite nanoparticles; (B) nanoparticles prepared by sol-gel method.

The crystallite sizes were estimated by the peak broadening effect as implemented in BGMN. The results of Rietveld optimization are indicated in Table 2 and in Figure 2. Sizes of 7.9 nm and 10.2 nm were obtained for the $\text{Ca}_{0.5}\text{Mn}_{0.5}\text{Fe}_2\text{O}_4$ (citrate-stabilized) and $\text{Ca}_{0.5}\text{Mn}_{0.5}\text{Fe}_2\text{O}_4$ (sol-gel) NPs, respectively. For the case of the citrate-stabilized NPs, better fits were obtained for cation distributions that placed Ca^{2+} in octahedral sites. The obtained lattice parameter of 0.8427 nm is larger than the value of 0.8387 reported for MnFe_2O_4 produced by a hydrothermal procedure [29]. This shows that an expansion of the crystal structure occurs in order to accommodate the Ca^{2+} ions.

Table 2. Calculated R_p and χ^2 parameters, phase sizes and percentages obtained by Rietveld refinement of X-ray diffraction patterns of $\text{Ca}_{0.5}\text{Mn}_{0.5}\text{Fe}_2\text{O}_4$ nanoparticles stabilized by citrate (A) or obtained through the sol–gel technique (B). i is the degree of inversion; f_{Ca}^T is the fraction of Ca^{2+} in tetrahedral sites.

Sample	$O_{x,y,z}$ (*)	i	f_{Ca}^T	Phase Size (nm)	Lattice Constant (nm)	Hematite (wt%)	R_p	χ^2
A	0.3816	1	0	7.6	0.8427	-	9.19	1.26
	0.3819	0.5 (+)	0	7.5	0.8427		9.20	1.26
	0.3795	0.5 (+)	1 (+)	7.7	0.8430		9.47	1.33
	0.3780	0 (+)	1 (+)	7.7	0.8531		9.48	1.33
B	0.3848	1	0	10.2	0.8374	27.3	9.43	1.57

(*) Value of $O_{x,y,z}$ in CIF file 2300618 is 0.25053 (+) fixed.

3.1.2. Scanning Electron Microscopy (SEM)

The SEM images of $\text{Ca}_{0.5}\text{Mn}_{0.5}\text{Fe}_2\text{O}_4$ nanoparticles are presented in Figure 3. A Gaussian distribution was fitted to the experimental data and populations of 9.1 ± 2.4 nm and 11.5 ± 4.3 nm were obtained, respectively, for the citrate-stabilized NPs (Figure 3A) and NPs obtained by sol–gel method (Figure 3B). These size values are in very good agreement with XRD results. The small and uniform population of the citrate-stabilized NPs, with low size distributions, emphasizes the role of citrate, which demonstrated an important role in the synthesis of ferrite nanoparticles, allowing for a homogeneous mixing of metal cations while retarding particle growth via the formation of surface citrate complexes, inhibiting the agglomeration of the NPs [30,31]. Some particle aggregation observed in the images is due to the technique employed, which requires a dry film of the sample in a solid grid with subsequent application of a vacuum. This procedure causes the aggregation of the nanostructures in the grid and, thus, in SEM images.

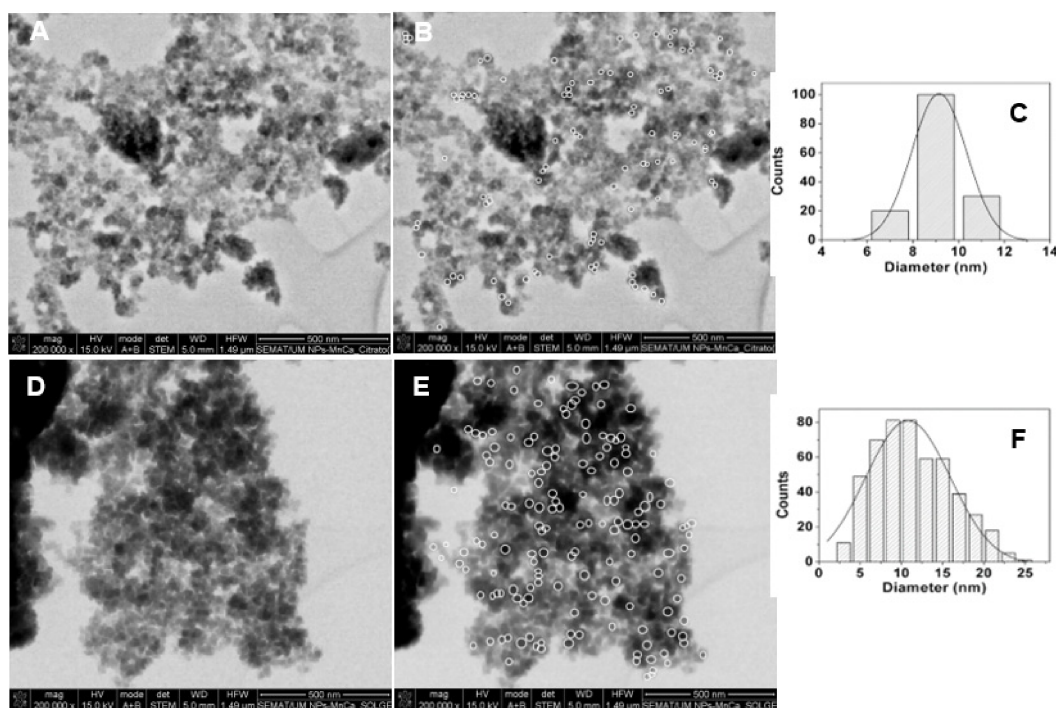


Figure 3. STEM images of (A) citrate-stabilized nanoparticles and (B) citrate-stabilized nanoparticles with the nanoparticles selected by *Image J* software (white circles); (C) Histogram of size distribution of citrate-stabilized nanoparticles. STEM images of (D) nanoparticles prepared by sol–gel and (E) nanoparticles prepared by sol–gel with the nanoparticles selected by *Image J* software (white circles); (F) Histogram of size distribution of nanoparticles prepared by sol–gel.

3.1.3. Sedimentation Kinetics

The colloidal stability of the nanoparticles is an important parameter for biomedical applications. Hence, the sedimentation profile of suspensions of the prepared nanoparticles is crucial in determining their stability. Different concentrations of the prepared nanoparticles, 0.2%, 0.1%, 0.05% and 0.025% (% m/v), were studied. The deposition rate was determined through the sedimentation kinetics, which was obtained measuring the absorbance of nanoparticles suspensions within 15 min intervals, for 3 h (Figure 4). The experimental results follow first-order kinetics and the sedimentation rates were estimated by fitting the Becquerel decay function or compressed hyperbola to the sedimentation profiles at different concentrations (insets of Figure 4). Becquerel's decay law is given by Equation (3),

$$I(t) = \frac{1}{\left[1 + \frac{ct}{\tau_0}\right]^{1/c}} \quad (3)$$

where the control parameter c is taken as $0 < c < 1$, and τ_0 has dimensions of time [32].

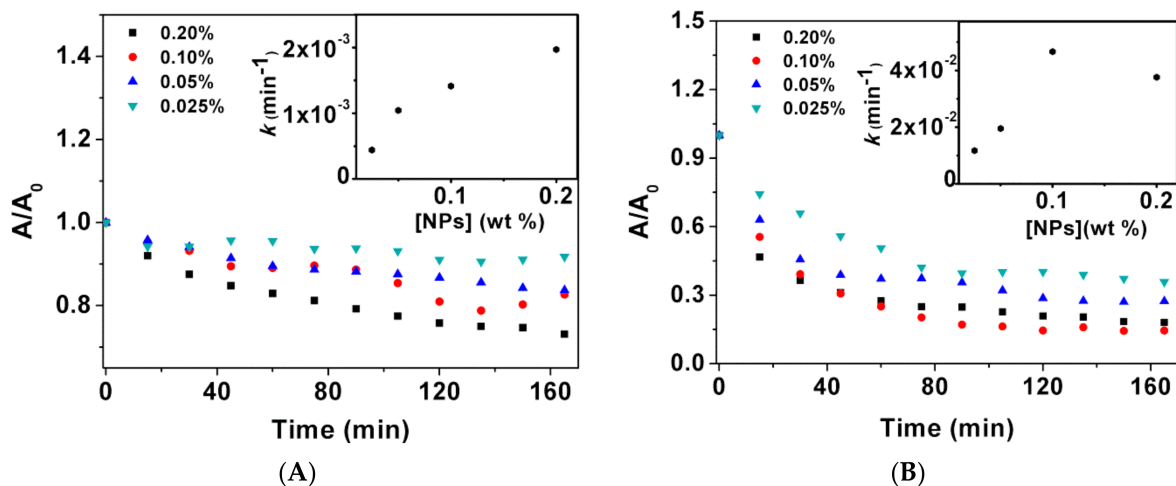


Figure 4. Sedimentation profiles of (A) citrate-stabilized nanoparticles; (B) Nanoparticles prepared by sol-gel. Insets: sedimentation rate dependence on nanoparticle concentration.

Both types of nanoparticles (synthesized by the two different methods) were shown to be stable, with sedimentation behavior suggesting the occurrence of nanoparticle aggregation into stable agglomerates which settle down at a faster rate than single nanoparticles [33]. Within the range of concentrations studied, the deposition of the citrate-stabilized NPs shows a linear trend with increasing concentration. On the other hand, the NPs prepared by sol-gel revealed a faster decay over time, with no linear dependence with the NP concentration. The citrate-stabilized NPs display higher stability for the largest concentration studied, with a deposition rate of $1.98 \times 10^{-3} \text{ min}^{-1}$ for 0.2 wt%, while sol-gel NPs show a rate of $3.94 \times 10^{-2} \text{ min}^{-1}$ for the same nanoparticle concentration. The three carboxyl groups in every citrate ion and the repulsive forces between the electric charges of the radical ions make the nanoparticles more water-dispersible, providing electrostatic stabilization [34].

3.1.4. Magnetic Properties

Ferrite nanoparticles typically have a spinel-type crystal structure with a general formula (A)[B]₂O₄, where (A) denotes tetrahedral sites and [B] the octahedral sites. Each unit cell is composed of eight formula units, where the larger oxygen anions enclose a face-centered-cubic structure with the smaller cations in the interstitial sites, that is, (A)-sites and [B]-sites (Figure 5). The cation distribution in the (A)-sites and [B]-sites, the magnetic interaction between the magnetic moments of the metal ions, and their relative ion strength determine the magnetic behavior of the nanoparticles.

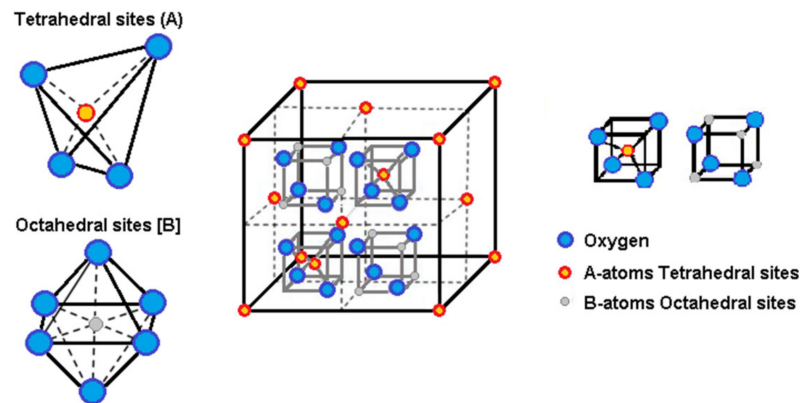


Figure 5. Representation of the crystal cell lattice, with the representation of the A-sites and B-sites.

The spinel structure of the mixed calcium/manganese ferrite can be written as $(\text{Ca}_x^{2+}\text{Mn}_y^{2+}\text{Fe}_{1-x-y}^{3+}) [\text{Ca}_{0.5-x}^{2+}\text{Mn}_{0.5-y}^{2+}\text{Fe}_{1+x+y}^{3+}] \text{O}_4^{2-}$, where $(1-x-y)$ denotes the inversion degree corresponding to the fraction of (A)-sites that are occupied by Fe^{3+} [35]. In an inverted spinel ferrite, one-half of Fe^{3+} is placed in (A)-sites and the other half in [B]-sites, mutually compensating their magnetic moments. Thus, the resulting magnetic moment of the ferrite is due to the magnetic moment of bivalent cations (Me^{2+}) in [B]-sites [36]. According to XRD analysis, an octahedral site preference of Ca^{2+} was observed, from either a completely inverted structure or a structure with an inversion degree of 0.5 and Mn^{2+} only in (A)-sites (Table 3). Hence, the spinel structure takes either the formula $(\text{Fe}^{3+}) [\text{Ca}_{0.5}^{2+}\text{Fe}^{3+}] \text{O}_4^{2-}$ or $(\text{Mn}_{0.5}^{2+}\text{Fe}_{0.5}^{3+}) [\text{Ca}_{0.5}^{2+}\text{Fe}_{1.5}^{3+}] \text{O}_4^{2-}$. Bulk MnFe_2O_4 is a partially inverted spinel structure, with a typical small inversion parameter of 0.2 and a corresponding formula $(\text{Mn}_{0.8}^{2+}\text{Fe}_{0.2}^{3+}) [\text{Mn}_{0.2}^{2+}\text{Fe}_{1.8}^{3+}] \text{O}_4^{2-}$. This is originated from the similar site preferences of Mn^{2+} and Fe^{3+} , as both have similar sizes and d-orbital energy and occupation (d^5) [37]. Therefore, the most probable configuration for the synthesized $\text{Ca}_{0.5}\text{Mn}_{0.5}\text{Fe}_2\text{O}_4$ nanoparticles is $(\text{Mn}_{0.5}^{2+}\text{Fe}_{0.5}^{3+}) [\text{Ca}_{0.5}^{2+}\text{Fe}_{1.5}^{3+}] \text{O}_4^{2-}$.

Table 3. Saturation magnetization (M_s), remnant magnetization (M_r), M_r/M_s ratio and coercive field (C) for $\text{Ca}_{0.5}\text{Mn}_{0.5}\text{Fe}_2\text{O}_4$ nanoparticles, at room temperature.

	M_s (emu/g)	M_r (emu/g)	M_r/M_s	C (Oe)
Citrate-stabilized $\text{Ca}_{0.5}\text{Mn}_{0.5}\text{Fe}_2\text{O}_4$	53.91	0.95	0.02	13.90
$\text{Ca}_{0.5}\text{Mn}_{0.5}\text{Fe}_2\text{O}_4$ prepared by sol–gel	26.68	3.88	0.15	96.77

The magnetic dependence on the applied magnetic field of the citrate-stabilized $\text{Ca}_{0.5}\text{Mn}_{0.5}\text{Fe}_2\text{O}_4$ NPs and those prepared by sol–gel was measured and the corresponding hysteresis loops are shown on Figure 6. The obtained saturation magnetization and hysteresis parameters are summarized in Table 3.

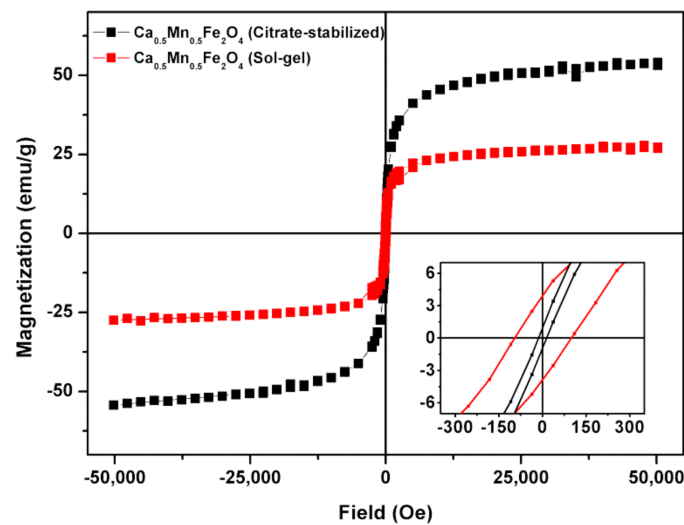


Figure 6. Hysteresis loops of citrate-stabilized $\text{Ca}_{0.5}\text{Mn}_{0.5}\text{Fe}_2\text{O}_4$ NPs and $\text{Ca}_{0.5}\text{Mn}_{0.5}\text{Fe}_2\text{O}_4$ NPs prepared by sol-gel, at room temperature. Inset: Low region field enlargement.

Both types of $\text{Ca}_{0.5}\text{Mn}_{0.5}\text{Fe}_2\text{O}_4$ nanoparticles show no hysteresis, with very low values of remnant magnetization and coercive field (Table 3). The citrate-stabilized NPs are superparamagnetic, with a magnetic squareness value below 0.1, indicating the loss of more than 90% of magnetization upon the removal of the applied field. On the other hand, NPs obtained by sol-gel are at the limit for ferromagnetic behavior. A high saturation magnetization of 53.91 emu/g was obtained for the crystalline $\text{Ca}_{0.5}\text{Mn}_{0.5}\text{Fe}_2\text{O}_4$ citrate-stabilized nanoparticles, while poor magnetization was observed for the NPs obtained by sol-gel. The lower magnetization value of the nanoparticles synthesized by the sol-gel method can be justified by the presence of an additional phase of hematite (as detected in XRD diffractogram) which is very weakly magnetic.

According to Neel's sub-lattice field model [7], the A-B exchange interaction is stronger than the A-A or B-B interaction and the saturation magnetization (M_s) can be estimated by the relation $M_s = M_B - M_A$, where M_B and M_A are the magnetization of [B]- and (A)-sites, respectively. Taking the magnetic moment of $5\mu_B$ for the cations Mn^{2+} e Fe^{3+} (both with five unpaired d-electrons) and $0\mu_B$ for Ca^{2+} , the magnetic moment per formula unit of the $(\text{Mn}_{0.5}^{2+}\text{Fe}_{0.5}^{3+}) [\text{Ca}_{0.5}^{2+}\text{Fe}_{1.5}^{3+}] \text{O}_4^{2-}$ configuration is given by $[(\text{Ca}^{2+}\uparrow 0.5 \times 0\mu_B) + (\text{Fe}^{3+}\uparrow 1.5 \times 5\mu_B)] - ((\text{Mn}^{2+}\downarrow 0.5 \times 5\mu_B) + (\text{Fe}^{3+}\downarrow 0.5 \times 5\mu_B)) = 2.5\mu_B$. On the other hand, assuming the typically small inversion parameter of manganese ferrite nanoparticles ($i = 0.2$), the expected magnetic moment per formula unit is $[(\text{Mn}^{2+}\uparrow 0.2 \times 5\mu_B) + (\text{Fe}^{3+}\uparrow 1.8 \times 5\mu_B)] - ((\text{Mn}^{2+}\downarrow 0.8 \times 5\mu_B) + (\text{Fe}^{3+}\downarrow 0.2 \times 5\mu_B)) = 5\mu_B$. Hence, a reduction in the magnetization for the $\text{Ca}_{0.5}\text{Mn}_{0.5}\text{Fe}_2\text{O}_4$ nanoparticles should be expected by the Neel's sub-lattice field model. Yet, Wang et al. have prepared MnFe_2O_4 NPs with a saturation magnetization of 53.6 emu/g, using a synthesis process that resulted in nanoparticles with comparable crystalline sizes around 11.4 nm and a lattice parameter of 0.8387 nm [29]. Contrary to expectations, the magnetization reported by Wang for MnFe_2O_4 NPs is very similar to that obtained in this work for the citrate-stabilized $\text{Ca}_{0.5}\text{Mn}_{0.5}\text{Fe}_2\text{O}_4$ NPs (53.91 emu/g, Table 3). In addition, the increase in the lattice parameter from 0.8387 nm (MnFe_2O_4 NPs) to 0.8427 nm ($\text{Ca}_{0.5}\text{Mn}_{0.5}\text{Fe}_2\text{O}_4$, Table 2) points to a structural distortion that could disrupt the perfect alignment of spins from the A and B sites, leading to a possible increase in the effective magnetic moment. The lattice parameter increases and the Ca^{2+} octahedral site preference is supported by the larger ionic radius of the cation Ca^{2+} (0.99 Å contrasting with 0.80 Å of the Mn^{2+} , and 0.64 Å of the Fe^{3+} , for coordination 6 in octahedral position [38]). The influence of structural distortions in effective magnetic moment was also suggested by Y. Wang et al. for the case of rare-earth-doped calcium manganite perovskites [39]. Hence,

the high magnetization of mixed calcium/manganese ferrite NPs could be related to the distortion that augments the magnetic moment of the system.

3.2. Magnetoliposome Characterization by DLS and SEM

Considering the best structural and magnetic properties of the citrate-stabilized nanoparticles obtained by co-precipitation, these NPs were chosen for the preparation of magnetic liposomes. The thermosensitive lipid DPPC (dipalmitoylphosphatidylcholine), possessing a transition (melting) temperature at 41 °C [40], around the ones used in mild hyperthermia therapy, was chosen as the main component of the formulation. As tumor cells have a lower pH than non-tumor cells, the pH-sensitive lipid CHEMS (cholesteryl hemisuccinate) [41,42] was included in the nanosystems, with the purpose of attaining a pH-triggered release. Poly(ethylene glycol) (PEG) was also incorporated in the magnetoliposomes (through the PEGylated lipid DSPE-PEG) to ensure prolonged systemic circulation by avoiding clearance by the immune system.

Electrophoretic light scattering measurements (determination of zeta potential) were performed at neutral and acidic pH, respectively 7.4 and 5, to investigate the pH-sensitivity of the magnetic liposomal formulations containing the polymorphic molecule CHEMS. The results are displayed in Table 4. The zeta potential of DPPC magnetoliposomes (100%) at pH = 7.4 and pH = 5 is also shown, for comparison.

Table 4. Zeta potential values of the magnetic liposomes of several compositions, measured by electrophoretic light scattering.

Formulation	pH	Zeta Potential (mV)
DPPC (100%)	7.4	-1.83 ± 0.65
	5	-1.75 ± 0.82
DPPC:CHEMS (80:20)	7.4	-26.7 ± 1.10
	5	-0.73 ± 0.9
DPPC:CHEMS:DSPE-PEG (80:20:0.4)	7.4	-17.0 ± 0.9
	5	-2.55 ± 0.89

DPPC magnetoliposomes are very slightly negative, due to the surface charge of citrate-coated magnetic nanoparticles. A value of -25.5 mV was reported for the zeta potential of citrate-coated magnetite at pH = 6, decreasing with increasing pH [43]. At neutral pH, the presence of CHEMS in the magnetoliposomes formulations of DPPC:CHEMS and DPPC:CHEMS:DSPE-PEG reinforces the negative surface charge, as the succinate head-group is deprotonated at neutral pH (pK~5.8 [14]). The more negative zeta-potential value of -26.7 ± 1.10 mV for the magnetoliposomes of DPPC:CHEMS indicates an outermost location of the CHEMS molecule in this formulation. At acidic pH, below its pK value, the protonation of CHEMS leads to a decrease in zeta potential to a very slight negative charge (near neutral) of -0.73 ± 0.9 mV and -2.55 ± 0.89 mV for DPPC:CHEMS and DPPC:CHEMS:DSPE-PEG, respectively (Table 4). Additionally, the protonation of CHEMS enhances the formation of the hexagonal phase (H_{II}), conferring a more fusogenic character to the nanosystems at this pH. Hence, it is possible to conclude that the magnetoliposomes of DPPC:CHEMS and DPPC:CHEMS:DSPE-PEG are pH-sensitive, being suitable for pH-triggered release of encapsulated drugs in the acidic tumor microenvironment.

The interaction of the magnetic liposomes with small unilamellar vesicles (SUVs) of Egg-PC (L- α -lecithin from egg yolk), here employed as biomembrane models, was monitored by dynamic light scattering (DLS), investigating their fusion capabilities under neutral and acidic pH. For that, the hydrodynamic diameters of magnetoliposomes (MLs), SUVs and the mixture of both nanosystems (after stabilizing 10 min) were measured at pH = 7.4 (PBS buffer) and pH = 5 (acetate buffer). The outcomes of this experiment are shown in Table 5.

Table 5. Hydrodynamic diameter and polydispersity index (PdI) values of magnetic liposomes, SUVs and the mixture of both nanosystems, measured by dynamic light scattering (DLS).

Formulation	Hydrodynamic Size (nm)		PdI	
	pH = 7.4	pH = 5	pH = 7.4	pH = 5
SUVs	96.5 ± 2.4	92.3 ± 12	0.27 ± 0.01	0.27 ± 0.01
MLs (DPPC:CHEMS)	149.9 ± 17	203.6 ± 10	0.29 ± 0.01	0.27 ± 0.04
SUVs + MLs (DPPC:CHEMS)	171.6 ± 2.2	597.3 ± 58	0.25 ± 0.01	0.29 ± 0.04
MLs (DPPC:CHEMS:DSPE-PEG)	213.2 ± 1.1	225.6 ± 19	0.24 ± 0.001	0.28 ± 0.002
SUVs + MLs (DPPC:CHEMS:DSPE-PEG)	336.1 ± 121	376.1 ± 66	0.24 ± 0.027	0.25 ± 0.050

In general, the formation of generally monodisperse systems ($PdI < 0.3$) can be observed. The small hydrodynamic diameters of Egg-PC SUVs, at both pH 7.4 and 5, are in accordance with previous values reported for this type of vesicle [44]. At neutral pH, hydrodynamic sizes below or around 200 nm were measured, suitable for therapeutic applications considering that the enhanced permeation and retention (EPR) effect is guaranteed for nanocarriers' sizes lower than 400 nm, while being more effective at diameters below 200 nm [45]. The larger negative surface charges (at pH = 7.4) of DPPC:CHEMS MLs (Table 4) contribute to a reduction in the mean size of this magnetic liposomal formulation, owing to a decrease in aggregation promoted by electrostatic repulsions.

An increase in size was observed for the mixture containing SUVs and MLs, supporting the fusion between the two types of nanostructures. As expected, in an acidic environment, the increase in size was even more pronounced, due to the lamellar-to-inverted hexagonal phase transition of CHEMS that supports membrane fusion at pH 5. The MLs of DPPC:CHEMS were the best candidates for pH-sensitive fusion with the largest size difference for the mixture of SUVs and MLs at pH 7.4 and 5. The lower increase obtained for the mixture of SUVs and MLs of DPPC:CHEMS:DSPE-PEG, at pH = 5, may be related to PEG molecules forming a hydrophilic corona that suppressed membrane fusion. In fact, PEGylation have shown poor endosomal escape through membrane fusion and lack of loaded molecules release in lysosomes [46]. However, recent studies have shown that the use of cleavable PEG derivatives, which are easy to break under pathological conditions, can facilitate the membrane fusion while keeping the extended drug circulation time [47].

Scanning electron microscopy (SEM) was used for the morphological assessment of the developed MLs. Despite not being ideal for analyzing liposomes, as it requires sample drying or fixing, SEM can provide general information on the concentric structure, as well as give details on size and spherical morphology [48]. An SEM image of the MLs based on citrate-stabilized nanoparticles is displayed in Figure 7A.

In general, single-layer magnetic liposomes with spherical shape and diameters around 100 nm were obtained. As expected, these results reveal slightly smaller diameters than the size distribution obtained from the DLS measurements, as the latter comprise the liquid layer around the nanosystem, while SEM measures the size of the dry nanoparticles. Additionally, aggregation in aqueous media can lead to larger average sizes. On the other hand, the fragmented and smaller size structures may result from the perturbation from the high-vacuum conditions required for sample preparation in SEM. A TEM image in Figure 7B illustrates a single magnetoliposome, evidencing the presence of magnetic nanoparticles with sizes smaller than 10 nm.

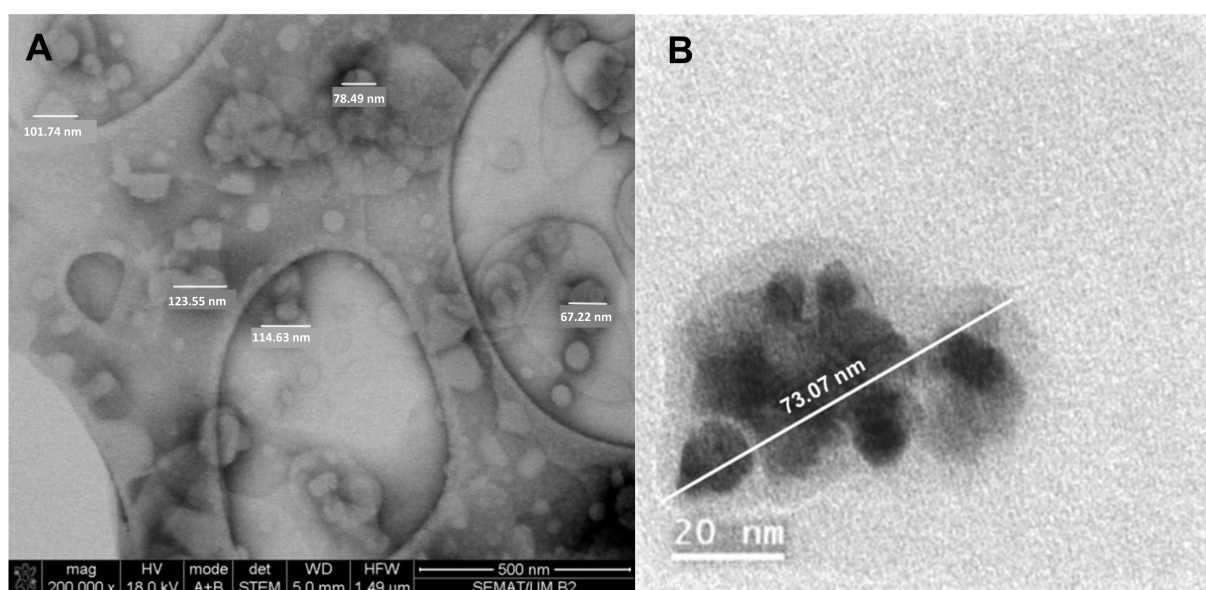


Figure 7. (A) SEM image of magnetoliposomes of DPPC (100%) based on citrate-stabilized nanoparticles, showing spherical structures around 100 nm size. (B) TEM image of a magnetoliposome.

3.3. Drug-Loaded Magnetic Liposomes

3.3.1. New Antitumor Thienopyridine Derivatives

As other thienopyridine derivatives previously synthesized and described [18–22], Compounds A and B are fluorescent in several solvents (except in water). This is an advantage for monitoring the incorporation of these compounds in the developed magnetic bionanosystems, as fluorescence provides a versatile method allowing for the determination of lower concentrations than UV-Visible absorption spectroscopy.

Considering these properties, UV-Vis absorption and fluorescence measurements were carried out for both compounds in different solvents and fluorescence quantum yields were estimated. The maximum absorption and emission wavelengths, molar absorption coefficients and fluorescence quantum yields are displayed in Table 6. Compound B is more fluorescent than Compound A, with quantum yields between 5% and 10%, while Compound A presents emissive quantum yields around 2%. Normalized fluorescence spectra are presented in Figure 8, with examples of absorption spectra as insets. A general red shift in polar and protic solvents (acetonitrile, ethanol) can be observed, together with a loss of vibrational structure and band enlargement, especially for Compound B, indicative of the intramolecular charge transfer character of the excited state [26]. This behavior points to a moderate sensitivity of the compounds' emission to the environment.

Table 6. Maximum absorption (λ_{abs}) and emission (λ_{em}) wavelengths, molar absorption coefficient values (ϵ) and fluorescence quantum yields (Φ_{F}) calculated for Compounds A and B (*sh*: shoulder).

Solvent	$\lambda_{\text{abs}}/\text{nm}$ ($\epsilon/10^5 \text{ M}^{-1} \text{ cm}^{-1}$)		$\lambda_{\text{em}}/\text{nm}$		Φ_{F}	
	Compound A	Compound B	Compound A	Compound B	Compound A	Compound B
Ethyl acetate	338 (1.37)	348 (2.07)	371; 387	401	0.016	0.05
Chloroform	338 (1.39)	352 (1.73)	375; 392	406	0.020	0.08
Acetonitrile	338 (1.27)	348 (1.79)	371; 385 (<i>sh</i>)	410	0.017	0.05
Ethanol	338 (1.24)	350 (1.76)	375; 389 (<i>sh</i>)	421	0.018	0.10

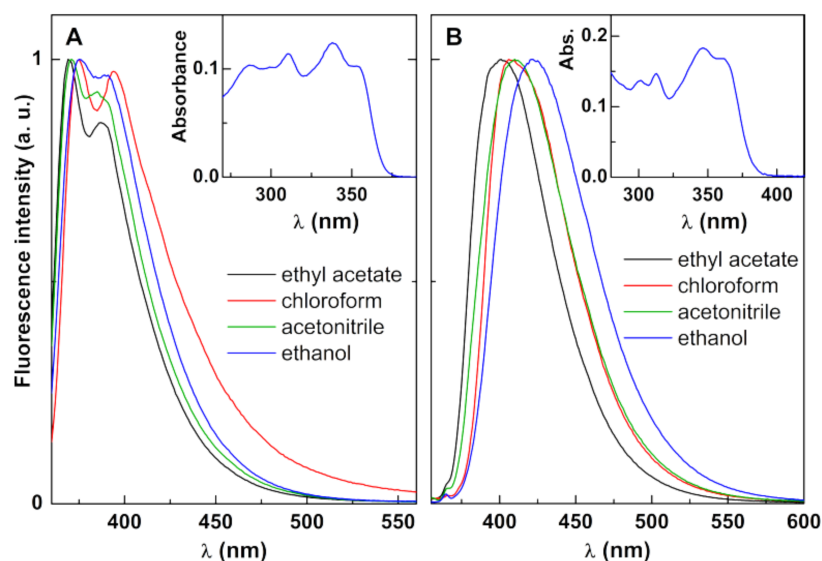


Figure 8. Normalized fluorescence spectra of 1×10^{-6} M solutions of Compounds (A) ($\lambda_{exc} = 350$ nm) and (B) ($\lambda_{exc} = 330$ nm) in different solvents. Insets: Absorption spectra in ethanol, as examples.

The photophysical characterization of Compounds A and B (Figure 8 and Table 6) in several solvents is important to understand: not only are the compounds fluorescent in different environments, but their emission is also sensitive to the surrounding media. Understanding this will allow for determining compound encapsulation efficiencies and localization in magnetoliposomes—relevant parameters to be considered when assessing a nanocarrier performance.

3.3.2. Magnetic Liposomes with Encapsulated Drugs

The antitumor Compounds A and B were loaded in magnetoliposomes by co-injection with the lipids the formulation. The encapsulation of Compounds A and B can be followed by fluorescence emission, taking into account the usual fluorescence quenching promoted by the magnetic nanoparticles. In Figure 9, a strong fluorescence inhibition is observed for both compounds when compared with the emission in neat liposomes (in the absence of the magnetic component). This behavior is common to all the lipid formulations studied and was already reported in previous works with other encapsulated drugs (including different thienopyridine derivatives) in magnetoliposomes [21,22,49].

Fluorescence anisotropy measurements are also useful in estimating the main location of the potential drugs in the nanocarriers (Table 7). In fact, fluorescence anisotropy, r , is related to the microviscosity, η , of the environment, through Equation (4) [26],

$$\frac{1}{r} = \frac{1}{r_0} \left(1 + \frac{\tau}{\tau_c} \right), \quad (4)$$

where r_0 is the fundamental anisotropy, τ is the excited-state lifetime of the fluorophore, and τ_c is the rotational correlation time, given by $\tau_c = (V_h \eta) / (k_B T)$, and with being V_h the hydrodynamic volume, k_B the Boltzmann's constant and T the absolute temperature. The fundamental anisotropy can be estimated from the value in a very viscous solvent (e.g., glycerol).

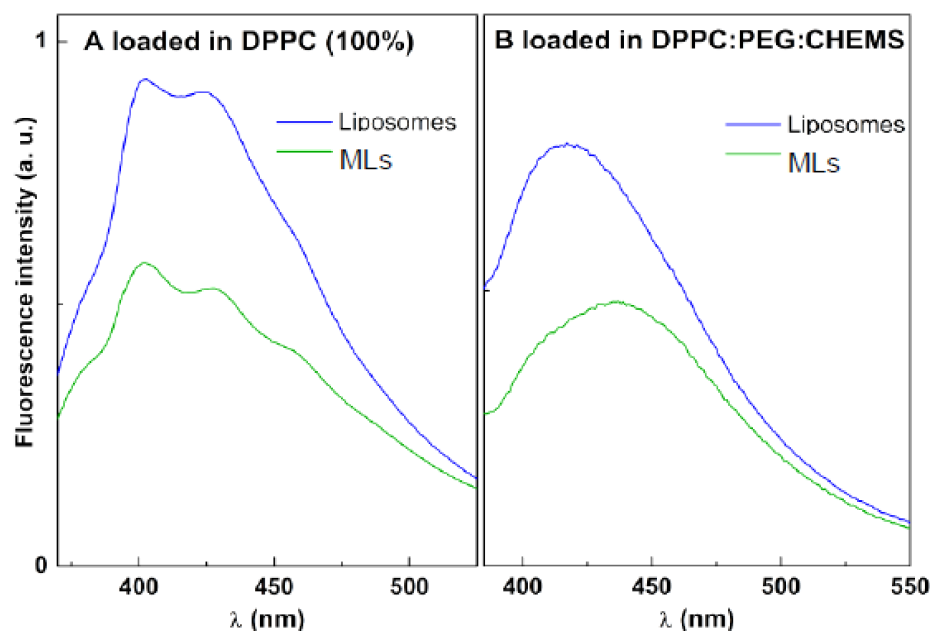


Figure 9. Fluorescence spectra of compounds loaded in liposomes and magnetic liposomes (A): Compound A loaded in DPPC (100%); (B): Compound B loaded in DPPC:PEG:CHEMS (80:20:0.4).

Table 7. Fluorescence anisotropy values of Compounds A and B in magnetic liposomes (MLs).

System	Formulation	Compound A	Compound B
MLs	DPPC	0.08 (25 °C)	0.03 (25 °C)
		0.06 (55 °C)	0.02 (55 °C)
	DPPC:CHEMS	0.14 (25 °C)	0.14 (25 °C)
		0.10 (55 °C)	0.11 (55 °C)
	DPPC:CHEMS: DSPE-PEG	0.11 (25 °C)	0.14 (25 °C)
		0.07 (55 °C)	0.12 (55 °C)
Glycerol	-	0.33 (25 °C)	0.30 (25 °C)

In Table 7, a general decrease in anisotropy can be observed when the temperature is higher (55 °C) than that of the DPPC phase transition. This indicates that Compounds A and B detect the transition of the lipid bilayer (from gel to the liquid-crystalline phase) and, therefore, are mainly located in the membrane. An increase in the steady-state anisotropy values is predicted from the decrease in the excited-state lifetime (according to Equation (4)). When the temperature is raised from 25 °C to 55 °C, the excited-state lifetime decreases, owing to the enhancement of non-radiative deactivation pathways (especially the rate constant for internal conversion from the first singlet excited state to the ground state). However, a decrease in fluorescence anisotropy is observed, which can only be attributed to a decrease in the rotational correlation time of the fluorescent compound, which arises from the decrease in membrane microviscosity upon transition from the gel to the liquid-crystalline phase.

It should also be noticed that the compounds have very low anisotropy values in the DPPC (100%) formulation, and probably are in a hydrated and fluid environment in these nanostructures. On the other hand, CHEMS may facilitate compounds' penetration in the membranes, by fluidizing the DPPC rigid phase, as happens with cholesterol [50]. This is reflected by the higher anisotropy values in formulations containing CHEMS.

The encapsulation efficiencies of both antitumor compounds in the several magnetoliposomes formulations were determined and the results are presented in Table 8.

Table 8. Values of encapsulation efficiencies (in percentage) for the studied antitumor compounds loaded in DPPC magnetoliposomes (standard deviation is from three independent assays).

Nanosystem	Formulation	Compound A	Compound B
MLs	DPPC	99.1 ± 0.2	89.0 ± 3.0
	DPPC:CHEMS	98.6 ± 0.1	88.4 ± 2.8
	DPPC:CHEMS:DSPE-PEG	98.2 ± 0.2	91.2 ± 0.3

The encapsulation efficiencies, above 88%, for both compounds are very reasonable and no significant difference between the several MLs formulation were observed. Only for Compound B was a slight increase in encapsulation efficiency obtained for PEGylated MLs, indicating that this formulation is able to better retain this drug. Hence, at neutral pH, the lipid formulations of magnetic liposomes do not sufficiently affect membrane fluidity to influence compound encapsulation.

3.3.3. Förster Resonance Energy Transfer Assays

To further investigate whether the drug-loaded pH-sensitive MLs can deliver the encapsulated drug to model membranes (SUVs), Förster resonance energy transfer (FRET) assays were carried out using magnetoliposomes of DPPC:CHEMS and DPPC:CHEMS:DSPE-PEG loaded with Compound A. In these assays, this drug acts as the energy donor, while the hydrophobic dye curcumin in Egg-PC SUVs was used as energy acceptor. FRET occurs when a donor fluorophore in the excited state transfers its excitation energy to an acceptor moiety in the ground state through a non-radiative process. FRET between two fluorescent molecules is expected to be efficient if the donor–acceptor distance is below 100 Å [26].

Assuming that membrane fusion between MLs and SUVs promotes the approximation between Compound A (donor) and curcumin (acceptor) within this distance range, the fusogenic capability was assessed. The emission spectra of MLs loaded with Compound A and of the mixture containing both MLs loaded with Compound A and SUVs containing curcumin were measured, exciting only the donor at 350 nm. FRET efficiency, Φ_{FRET} , representing the proportion of donor molecules that have transferred their excess energy to acceptor molecules, was calculated by taking the ratio of the donor-integrated fluorescence intensities in the presence of acceptor (F_{DA}) and in the absence of acceptor (F_{D}), through Equation (5). Here, the spectrum of MLs loaded with Compound A was used to measure the emission of the donor in the absence of an acceptor, while the spectrum of the mixture of loaded MLs and SUVs incorporating curcumin was used as the donor emission in the presence of an acceptor.

$$\Phi_{\text{FRET}} = 1 - \frac{F_{\text{DA}}}{F_{\text{D}}} \quad (5)$$

In cells, the pH value drops from early endosomes (pH = 6.5) to late endosomes (pH = 6) and to lysosomes (pH = 4.5–5) [51]. The tumor microenvironment is also acidic. Considering the objective of obtaining pH-sensitive magnetoliposomes by the inclusion of CHEMS, together with temperature sensitivity promoted by DPPC, these assays were performed at pH = 7.4 (normal physiological pH) and 5 (pH of tumor environment), and at temperatures of 25 °C (below phase transition temperature of DPPC) and 45 °C (above DPPC transition and at mild hyperthermia condition). The results are summarized in Table 9.

Table 9. Values of energy transfer efficiencies (Φ_{FRET}), in percentage, at different pH and temperature conditions.

Formulation	pH	Temperature (°C)	Φ_{FRET} (%)
DPPC:CHEMS	7.4	25	10.9
		45	22.5
	5	25	23.5
		45	26.6
DPPC:CHEMS:DSPE-PEG	7.4	25	18.4
		45	26.9
	5	25	28.9
		45	35.3

At pH = 5, higher FRET efficiencies were obtained, indicating a higher fusion ability between the MLs and SUVs at acidic conditions. Cholesteryl hemisuccinate evidences the capability of adopting a lamellar structure upon hydration in alkaline or neutral media [15], promoting membrane fusion upon acidification, due to the preference of neutral form for the inverted hexagonal phase (H_{II}) [14]. Additionally, a rise in temperature also increases the interaction between both nanosystems, with a larger membrane fusion and subsequent shorter distance between Compound A and curcumin (higher Φ_{FRET}). The lipid DPPC undergoes the gel-to-liquid crystalline phase transition at 41 °C; hence, at 45 °C, the increased membrane fluidity is expected to enhance membrane fusion. The DPPC:CHEMS:DSPE-PEG formulation has similar fusogenic sensitivity to the environment, considering the larger difference in FRET efficiencies between normal conditions (neutral pH and room temperature) and tumor environment under hyperthermia treatment (acidic pH and higher temperature). Therefore, the PEGylated nanocarrier maintains the pH and thermo-sensitive capabilities. Overall, the MLs based on citrate-stabilized $\text{Ca}_{0.5}\text{Mn}_{0.5}\text{Fe}_2\text{O}_4$ nanoparticles are very promising for antitumor drug delivery promoted by an external trigger in cancer therapy.

4. Conclusions

In this work, $\text{Ca}_{0.5}\text{Mn}_{0.5}\text{Fe}_2\text{O}_4$ nanoparticles were synthesized by co-precipitation (in the presence of citrate) and by the sol–gel technique. XRD measurements confirmed a pure crystalline phase of $\text{Ca}_{0.5}\text{Mn}_{0.5}\text{Fe}_2\text{O}_4$ NPs prepared by the first method. These nanoparticles showed a high saturation magnetization of 53.91 emu/g and superparamagnetic properties.

Magnetoliposomes of DPPC:CHEMS and DPPC:CHEMS:DSPE-PEG based on citrate-stabilized $\text{Ca}_{0.5}\text{Mn}_{0.5}\text{Fe}_2\text{O}_4$ nanoparticles, with sizes around 100 nm, were prepared. The presence of CHEMS in the liposomal formulation granted pH-sensitivity to the nanosystem, with a very slight negative charge in an acidic environment and a higher negative zeta-potential value at neutral pH. High encapsulation efficiencies, above 88%, were obtained for two new antitumor thienopyridine derivatives in the magnetic liposomes. FRET assays confirmed that the drug-loaded magnetoliposomes of DPPC:CHEMS and DPPC:CHEMS:DSPE-PEG display a higher fusogenic capability at acidic pH and high temperature. Hence, we developed magnetoliposomes suitable for temperature and pH-triggered release of anticancer drugs in the tumor microenvironment in combination with magnetic hyperthermia.

Author Contributions: Conceptualization, A.R.O.R., P.J.G.C. and E.M.S.C.; methodology, A.R.O.R., M.J.R.P.Q. and E.M.S.C.; validation, A.R.O.R., B.G.A., A.M.P., J.P.A. and E.M.S.C.; formal analysis, B.C.R., C.A.R.A., B.C.A., J.M.R., A.P., A.M.P. and J.P.A.; investigation, B.C.R., C.A.R.A., B.C.A., J.M.R., A.P. and B.G.A.; writing—original draft preparation, A.R.O.R. and E.M.S.C.; writing—review and editing, A.R.O.R.; P.J.G.C.; E.M.S.C.; supervision, A.R.O.R., A.M.P., J.P.A., M.J.R.P.Q. and E.M.S.C.; project administration, P.J.G.C. All authors have read and agreed to the published version of the manuscript.

Funding: This research was funded by the Portuguese Foundation for Science and Technology (FCT) in the framework of the Strategic Funding of CF-UM-UP (UIDB/04650/2020) and through the research project PTDC/QUI-QFI/28020/2017 (POCI-01-0145-FEDER-028020), financed by the European Fund of Regional Development (FEDER), COMPETE2020, and Portugal 2020. J.M.R. acknowledges FCT, ESF (European Social Fund—North Portugal Regional Operational Program) and HCOP (Human Capital Operational Program) for a PhD grant (SFRH/BD/115844/2016).

Institutional Review Board Statement: Not applicable.

Informed Consent Statement: Not applicable.

Data Availability Statement: Not applicable.

Conflicts of Interest: The authors declare no conflict of interest.

References

1. Jain, R.K.; Stylianopoulos, T. Delivering nanomedicine to solid tumors. *Nat. Rev. Clin. Oncol.* **2010**, *7*, 653–664. [[CrossRef](#)] [[PubMed](#)]
2. El-Sawy, H.S.; Al-Abd, A.M.; Ahmed, T.A.; El-Say, K.M.; Torchilin, V.P. Stimuli-responsive nano-architecture drug-delivery systems to solid tumor micromilieu: Past, present, and future perspectives. *ACS Nano* **2018**, *12*, 10636–10664. [[CrossRef](#)] [[PubMed](#)]
3. Raza, A.; Rasheed, T.; Nabeel, F.; Hayat, U.; Bilal, M.; Iqbal, H.M.N. Endogenous and exogenous stimuli-responsive drug delivery systems for programmed site-specific release. *Molecules* **2019**, *24*, 1117. [[CrossRef](#)] [[PubMed](#)]
4. Mazzotta, E.; Tavano, L.; Muzzalupo, R. Thermo-Sensitive Vesicles in Controlled Drug Delivery for Chemotherapy. *Pharmaceutics* **2018**, *10*, 150. [[CrossRef](#)] [[PubMed](#)]
5. Khoee, S.; Karimi, M.R. Dual-drug loaded Janus graphene oxide-based thermoresponsive nanoparticles for targeted therapy. *Polymer* **2018**, *42*, 80–98. [[CrossRef](#)]
6. Slam, K.; Haque, M.; Kumar, A.; Hoq, A.; Hyder, F.; Hoque, S.M. Manganese Ferrite Nanoparticles (MnFe₂O₄): Size Dependence for Hyperthermia and Negative/Positive Contrast Enhancement in MRI. *Nanomaterials* **2020**, *10*, 2297. [[CrossRef](#)]
7. Loganathan, A.; Kumar, K. Effects on structural, optical, and magnetic properties of pure and Sr-substituted MgFe₂O₄ nanoparticles at different calcination temperatures. *Appl. Nanosci.* **2016**, *6*, 629–639. [[CrossRef](#)]
8. Cardoso, B.D.; Rodrigues, A.R.O.; Almeida, B.G.; Amorim, C.O.; Amaral, V.S.; Castanheira, E.M.S.; Coutinho, P.J.G. Stealth Magnetoliposomes Based on Calcium-Substituted Magnesium Ferrite Nanoparticles for Curcumin Transport and Release. *Int. J. Mol. Sci.* **2020**, *21*, 3641. [[CrossRef](#)]
9. Zhang, L.; Qin, Y.; Zhang, Z.; Fan, F.; Huang, C.; Lu, L.; Wang, C. Dual pH/reduction-responsive hybrid polymeric micelles for targeted chemo-photothermal combination therapy. *Acta Biomater.* **2018**, *75*, 371–385. [[CrossRef](#)]
10. Gu, H.; Um, S.; Qiu, G.; Liu, X.; Zhang, L.; Yuan, Y.; Astruc, D. Redox-stimuli-responsive drug delivery systems with supramolecular ferrocenyl-containing polymers for controlled release. *Coord. Chem. Rev.* **2018**, *364*, 51–85. [[CrossRef](#)]
11. Hegazy, M.; Zhou, P.; Wu, G.; Wang, L.; Rahoui, N.; Taloub, N.; Huang, Y. Construction of polymer coated core-shell magnetic mesoporous silica nanoparticles with triple responsive drug delivery. *Polym. Chem.* **2017**, *8*, 5852–5864. [[CrossRef](#)]
12. Stubbs, M.; McSheehy, P.M.; Griffiths, J.R.; Bashford, C.L. Causes and consequences of tumour acidity and implications for treatment. *Mol. Med. Today* **2000**, *6*, 15–19. [[CrossRef](#)]
13. Pereira Gomes, I.; Aparecida Duarte, J.; Chaves Maia, A.L.; Rubello, D.; Townsend, D.M.; Branco de Barros, A.L.; Leite, E.A. Thermosensitive Nanosystems Associated with Hyperthermia for Cancer Treatment. *Pharmaceutics* **2019**, *12*, 171. [[CrossRef](#)] [[PubMed](#)]
14. Hafez, I.M.; Cullis, P.R. Cholesteryl hemisuccinate exhibits pH sensitive polymorphic phase behavior. *Biochim. Biophys. Acta Biomembr.* **2000**, *1463*, 107–114. [[CrossRef](#)]
15. Ding, W.-X.; Qi, X.-R.; Li, P.; Maitani, Y.; Nagai, T. Cholesteryl hemisuccinate as a membrane stabilizer in dipalmitoylphosphatidylcholine liposomes containing saikosaponin-d. *Int. J. Pharm.* **2005**, *300*, 38–47. [[CrossRef](#)]
16. Rodrigues, J.M.; Buisson, P.; Pereira, J.M.; Pinheiro, I.M.; Fernández-Marcelo, T.; Vasconcelos, M.H.; Berteina-Raboin, S.; Queiroz, M.-J.R.P. Synthesis of novel 8-(het)aryl-6H-pyran[4',3':4,5]thieno[3,2-b]pyridines by 6-endo-dig cyclization of Sonogashira products and halolactonizations with Cu salts/NXS. Preliminary antitumor evaluation. *Tetrahedron* **2019**, *75*, 1387–1397. [[CrossRef](#)]
17. Queiroz, M.-J.R.P.; Calhelha, R.C.; Vale-Silva, L.; Pinto, E.; Nascimento, M.S.-J. Novel [6-(hetero)arylamino]thieno[3,2-b]pyridines: Synthesis and antitumoral activities. *Eur. J. Med. Chem.* **2010**, *45*, 5732–5738. [[CrossRef](#)]
18. Machado, V.A.; Peixoto, D.; Costa, R.; Froufe, H.J.C.; Calhelha, R.C.; Abreu, R.M.V.; Ferreira, I.C.F.R.; Soares, R.; Queiroz, M.-J.R.P. Synthesis, antiangiogenesis evaluation and molecular docking studies of 1-aryl-3-[(thieno[3,2-b]pyridin-7-ylthio)phenyl]ureas: Discovery of a new substitution pattern for type II VEGFR-2 Tyr kinase inhibitors. *Bioorg. Med. Chem.* **2015**, *23*, 6497–6509. [[CrossRef](#)]
19. Machado, V.A.; Peixoto, D.; Queiroz, M.-J.R.P.; Soares, R. Antiangiogenic 1-aryl-3-[3-(thieno[3,2-b]pyridin-7-ylthio)phenyl]ureas inhibit MCF-7 and MDA-MB-231 human breast cancer cell lines through PI3K/Akt and MAPK/Erk pathways. *J. Cell. Biochem.* **2016**, *117*, 2791–2799. [[CrossRef](#)]

20. Costa, C.N.C.; Hortelão, A.C.L.; Ramos, J.M.F.; Oliveira, A.D.S.; Calhella, R.C.; Queiroz, M.-J.R.P.; Coutinho, P.J.G.; Castanheira, E.M.S. A new antitumoral heteroarylaminothieno[3,2-*b*]pyridine derivative: Incorporation in liposomes and interaction with proteins monitored by fluorescence. *Photochem. Photobiol. Sci.* **2014**, *13*, 1730–1740. [[CrossRef](#)]
21. Rodrigues, A.R.O.; Almeida, B.A.; Rodrigues, J.M.; Queiroz, M.-J.R.P.; Calhella, R.C.; Ferreira, I.C.F.R.; Pires, A.; Pereira, A.M.; Araújo, J.P.; Coutinho, P.J.G.; et al. Magnetoliposomes as carriers for promising antitumor thieno[3,2-*b*]pyridin-7-arylamines: Photophysical and biological studies. *RSC Adv.* **2017**, *7*, 15352–15361. [[CrossRef](#)]
22. Rodrigues, A.R.O.; Mendes, P.M.F.; Silva, P.M.L.; Machado, V.A.; Almeida, B.G.; Araújo, J.P.; Queiroz, M.-J.R.P.; Castanheira, E.M.S.; Coutinho, P.J.G. Solid and aqueous magnetoliposomes as nanocarriers for a new potential drug active against breast cancer. *Coll. Surf. B* **2017**, *158*, 460–468. [[CrossRef](#)] [[PubMed](#)]
23. Rodrigues, A.R.O.; Gomes, I.T.; Almeida, B.G.; Araújo, J.P.; Castanheira, E.M.S.; Coutinho, P.J.G. Magnetoliposomes based on nickel/silica core/shell nanoparticles: Synthesis and characterization. *Mater. Chem. Phys.* **2014**, *148*, 978–987. [[CrossRef](#)]
24. Rodrigues, A.R.O.; Ramos, J.M.F.; Gomes, I.T.; Almeida, B.G.; Araújo, J.P.; Queiroz, M.-J.R.P.; Coutinho, P.J.G.; Castanheira, E.M.S. Magnetoliposomes based on manganese ferrite nanoparticles as nanocarriers for antitumor drugs. *RSC Adv.* **2016**, *6*, 17302–17313. [[CrossRef](#)]
25. Jaafar-Maalej, C.; Diab, R.; Andrieu, V.; Elaissari, A.; Fessi, H. Ethanol injection method for hydrophilic and lipophilic drug-loaded liposome preparation. *J. Liposome Res.* **2010**, *20*, 228–243. [[CrossRef](#)]
26. Valeur, B. *Molecular Fluorescence Principles and Applications*; Wiley: Weinheim, Germany, 2002.
27. Bergmann, J.; Friedel, P.; Kleeberg, R. *Commission on Powder Diffraction Newsletter*; Oak Ridge National Laboratory: Oak Ridge, TN, USA, 1998; pp. 5–8.
28. Döbelin, N.; Kleeberg, R. Profex: A graphical user interface for the Rietveld refinement program BGMN. *J. Appl. Crystallog.* **2015**, *48*, 1573–1580. [[CrossRef](#)]
29. Wang, W.; Ding, Z.; Zhao, X.; Wu, S.; Li, F.; Yue, M.; Liu, J.P. Microstructure and magnetic properties of MFe₂O₄ (M = Co, Ni, and Mn) ferrite nanocrystals prepared using colloid mill and hydrothermal method. *J. Appl. Phys.* **2015**, *117*, 17A328. [[CrossRef](#)]
30. Bastús, N.G.; Merkoçi, F.; Piella, J.; Puentes, V. Synthesis of Highly Monodisperse Citrate-Stabilized Silver Nanoparticles of up to 200 nm: Kinetic Control and Catalytic Properties. *Chem. Mater.* **2014**, *13*, 2836–2846. [[CrossRef](#)]
31. Kim, S.G.; Wang, W.N.; Iwaki, T.; Yabuki, A.; Okuyama, K. Low-Temperature Crystallization of Barium Ferrite Nanoparticles by a Sodium Citrate-Aided Synthetic Process. *J. Phys. Chem. C* **2007**, *111*, 10175–10180. [[CrossRef](#)]
32. Foderà, V.; Donald, A. Tracking the heterogeneous distribution of amyloid spherulites and their population balance with free fibrils. *Eur. Phys. J. E* **2010**, *33*, 273–282. [[CrossRef](#)]
33. Veloso, S.R.S.; Silva, J.F.G.; Hilliou, L.; Moura, C.; Coutinho, P.J.G.; Martins, J.A.; Testa-Anta, M.; Salgueiriño, V.; Correa-Duarte, M.A.; Ferreira, P.M.T.; et al. Impact of Citrate and Lipid-Functionalized Magnetic Nanoparticles in Dehydropeptide Supramolecular Magnetogels: Properties, Design and Drug Release. *Nanomaterials* **2021**, *11*, 16. [[CrossRef](#)] [[PubMed](#)]
34. Hui, C.; Shen, C.; Yang, T.; Bao, L.; Tian, J.; Ding, H.; Gao, H.-J. Large-Scale Fe₃O₄ nanoparticle soluble in water synthesized by a facile method. *J. Phys. Chem. C* **2008**, *112*, 11336–11339. [[CrossRef](#)]
35. Bamzai, K.K.; Kour, G.; Kaur, B.; Kulkarni, S.D. Preparation, and Structural and Magnetic Properties of Ca Substituted Magnesium Ferrite with Composition MgCa_xFe_{2-x}O₄ (x = 0.00, 0.01, 0.03, 0.05, 0.07). *J. Mater.* **2014**, *2014*, 8. [[CrossRef](#)]
36. Mathew, D.S.; Juang, R.-S. An overview of the structure and magnetism of spinel ferrite nanoparticles and their synthesis in microemulsions. *Chem. Eng. J.* **2007**, *129*, 51–65. [[CrossRef](#)]
37. Grimes, R.W.; Anderson, A.B.; Heuer, A.H. Predictions of Cation Distributions in AB₂O₄ Spinel from Normalized Ion Energies. *J. Am. Chem. Soc.* **1989**, *111*, 1–7. [[CrossRef](#)]
38. Ahrens, L.H. The use of ionization potentials Part 1. Ionic radii of the elements. *Geochim. Cosmochim. Acta* **1952**, *2*, 155–169. [[CrossRef](#)]
39. Wang, Y.; Sui, Y.; Wang, X.; Su, W.; Liu, X. Correlation of structural distortion with magnetic properties in electron-doped Ca_{0.97}MnO₃ perovskites (R = rare-earth). *J. Appl. Phys.* **2010**, *108*, 063928. [[CrossRef](#)]
40. Lentz, B. Membrane ‘fluidity’ as detected by diphenylhexatriene probes. *Chem. Phys. Lipids* **1989**, *50*, 171–190. [[CrossRef](#)]
41. Chu, C.-J.; Szoka, F.C. pH-sensitive liposomes. *J. Liposome Res.* **1994**, *4*, 361–395. [[CrossRef](#)]
42. Massey, J.B. Effect of cholesteryl hemisuccinate on the interfacial properties of phosphatidylcholine bilayers. *Biochim. Biophys. Acta* **1998**, *1415*, 193–204. [[CrossRef](#)]
43. Nigam, S.; Barick, K.C.; Bahadur, D. Development of citrate-stabilized Fe₃O₄ nanoparticles: Conjugation and release of doxorubicin for therapeutic applications. *J. Magn. Magn. Mater.* **2011**, *323*, 237–243. [[CrossRef](#)]
44. Rodrigues, A.R.O.; Gomes, I.T.; Almeida, B.G.; Araújo, J.P.; Castanheira, E.M.S.; Coutinho, P.J.G. Magnetic liposomes based on nickel ferrite nanoparticles for biomedical applications. *Phys. Chem. Chem. Phys.* **2015**, *17*, 18011–18021. [[CrossRef](#)] [[PubMed](#)]
45. Deshpande, P.P.; Biswas, S.; Torchilin, V.P. Current trends in the use of liposomes for tumor targeting. *Nanomedicine* **2013**, *8*, 1509–1528. [[CrossRef](#)]
46. Yadav, D.; Dewangan, H.K. PEGylation: An important approach for novel drug delivery system. *J. Biomater. Sci. Polym. Ed.* **2021**, *32*, 266–280. [[CrossRef](#)] [[PubMed](#)]
47. Wawro, A.M.; Aoki, Y.; Muraoka, T. Enzymatically-cleavable traceless biotin tags for protein PEGylation and purification. *Chem. Commun. (Camb.)* **2018**, *54*, 1913–1916. [[CrossRef](#)] [[PubMed](#)]

48. Robson, A.-L.; Dastoor, P.C.; Flynn, J.; Palmer, W.; Martin, A.; Smith, D.W.; Woldu, A.; Hua, S. Advantages and Limitations of Current Imaging Techniques for Characterizing Liposome Morphology. *Front. Pharmacol.* **2018**, *9*, 80. [[CrossRef](#)] [[PubMed](#)]
49. Pereira, D.M.S.; Cardoso, B.D.; Rodrigues, A.R.O.; Amorim, C.O.; Amaral, V.S.; Almeida, B.G.; Queiroz, M.-J.R.P.; Martinho, O.; Baltazar, F.; Calhela, R.C.; et al. Magnetoliposomes containing calcium ferrite nanoparticles for applications in breast cancer therapy. *Pharmaceutics* **2019**, *11*, 477. [[CrossRef](#)]
50. Janoff, A.S.; Kurtz, C.L.; Jablonski, R.L.; Minchey, S.R.; Boni, L.T.; Gruner, S.M.; Cullis, P.R.; Mayer, L.D.; Hope, M.J. Characterization of cholesterol hemisuccinate and α -tocopherol hemisuccinate vesicles. *Biochim. Biophys. Acta* **1988**, *941*, 165–175. [[CrossRef](#)]
51. Mindell, J.A. Lysosomal acidification mechanisms. *Annu. Rev. Physiol.* **2012**, *74*, 69–86. [[CrossRef](#)]